Journal Pre-proof

On the broadband efficacy of impact absorbers

Tobias Weidemann, Luigi Carassale, Vincent Denoël, Malte Krack

PII: S0022-460X(23)00610-7
DOI: https://doi.org/10.1016/j.jsv.2023.118161
Reference: YJSVI 118161

To appear in: *Journal of Sound and Vibration*

Received date : 18 July 2023
Revised date : 19 October 2023
Accepted date : 10 November 2023

Please cite this article as: T. Weidemann, L. Carassale, V. Denoël et al., On the broadband efficacy of impact absorbers, *Journal of Sound and Vibration* (2023), doi: https://doi.org/10.1016/j.jsv.2023.118161.

This is a PDF file of an article that has undergone enhancements after acceptance, such as the addition of a cover page and metadata, and formatting for readability, but it is not yet the definitive version of record. This version will undergo additional copyediting, typesetting and review before it is published in its final form, but we are providing this version to give early visibility of the article. Please note that, during the production process, errors may be discovered which could affect the content, and all legal disclaimers that apply to the journal pertain.

© 2023 Published by Elsevier Ltd.

Journal Pre-proof
Click here to access/download;Manuscript;manuscript.tex
Click here to view linked References

On the broadband efficacy of impact absorbers

Tobias Weidemann[1], Luigi Carassale[2], Vincent Denoël[3], Malte Krack[1]

[1] *University of Stuttgart, GERMANY*

[2] *University of Genoa, ITALY*

[3] *University of Liège, BELGIUM*

Abstract

An impact absorber is a small, typically spherical, device placed freely into a cavity of the structure whose vibrations are to be mitigated. The device is particularly effective when it synchronizes with a target mode. The resulting strong impacts induce dissipation in the contact region and/or scattering of energy to and dissipation by high-frequency modes. As the synchronization can in principle take place at an arbitrary target frequency, impact absorbers are commonly claimed to have broadband efficacy. The present work reveals that this capacity is surprisingly limited. A taut string is considered under random excitation with a Gaussian-bell-curve-type power spectral density. It is shown that the fundamental mode dominates the displacement response even when the half power bandwidth spans only modes 29 to 37. Consequently, the absorber tends to synchronize with the fundamental mode, and energy is distributed to higher-frequency modes, reducing the displacement (root-mean-square) level. Even when the spectrum is cut off outside this bandwidth, or one of the high-order modes is subjected to harmonic near-resonant forcing, the fundamental mode is still prominent in the displacement response. In those cases, the reduction of the displacement level is marginal. Perhaps more critically, the energy transfer to high frequencies has a detrimental effect on the stress level, and the impacts cause sudden stress spikes, typically exceeding the linear limit cases (no / fixed absorber). Interestingly, the non-synchronized and less regular response typical for larger clearances is observed to trigger significant high-to-low energy transfer, which can have a beneficial effect on the stress level.

Keywords: vibro-impact; nonlinear energy sink; random vibration; vibration mitigation; targeted energy transfer

1. Introduction

Recently, an important shift of paradigm has occurred, as it was demonstrated that intentional use of substantial nonlinearities in dynamical systems and engineering structures can lead to significant improvement of their performance, opening new possibilities for design that simply would not be available in linear settings. An important example is the nonlinear Targeted Energy Transfer (TET), wherein vibration energy is directed from a source to a receiver (referred to as nonlinear energy sink - NES) in a nearly one-way, irreversible fashion [1]. Fast and intense TET can be realized also without dissipation in a local receiver/sink, but rather within the modal space of the system itself. This is achieved by adding appropriate strong nonlinearities within a system or structure, yielding scattering of vibration energy from low- to high-frequency modes. The efficacy of this inter-modal TET (IMTET) for passive vibration mitigation has been demonstrated analytically, computationally and experimentally [2, 3, 4, 5, 6].
A simple way to implement a strong nonlinearity is to place an additional mass freely into a casing of the host structure (Fig. 1-top-left) and letting it undergo collisions with the host structure (free-play nonlinearity). Impacts seem ideal for IMTET as they have the potential to scatter substantial vibration energy to extremely high-frequency modes on a very fast time scale. In the present work, IMTETis realized by introducing an additional, light device. It should be emphasized that IMTETcan also be implemented without introducing an additional degree of freedom, namely by adding only a nonlinear force element acting between existing degrees of freedom, or an existing degree of freedom and the ground. Depending on the behavior in the contact region, the described device acts as impact damper (ID) or Impact Energy Scatterer (IES), or a mixture of both. We may use the term *impact absorber* to refer to both, the ID and the IES. The distinction between these types of absorbers is their working principle. The ID relies on material

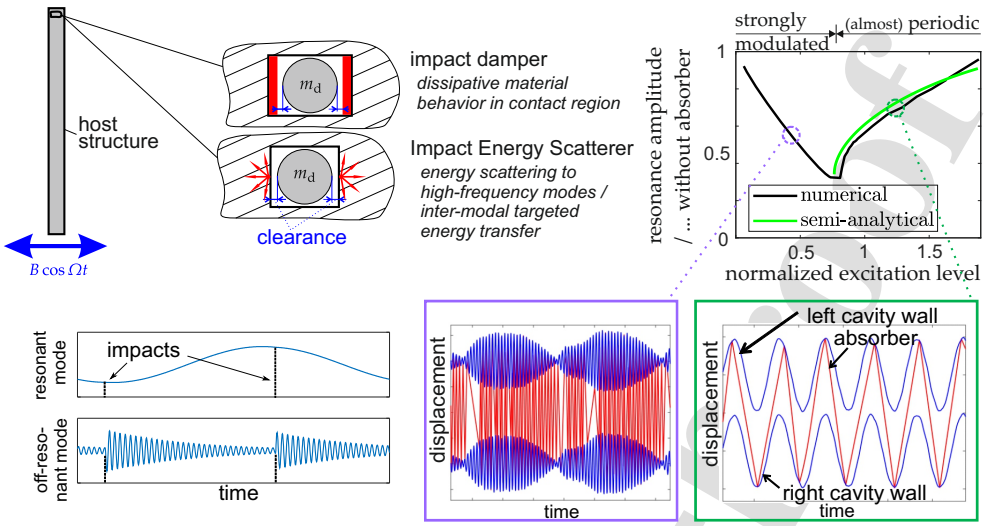

Figure 1: *Top-left:* Schematic illustration of a host structure with impact absorber (ID or IES). The region/flow of energy dissipation is highlighted in red to illustrate the main working principle of the two devices. *Top-right:* Resonant vibration amplitude normalized by that without absorber vs. normalized excitation level for an impact absorber. *Bottom-left:* Illustration of energy transfer to off-resonant (high-frequency) modes by the IES. *Bottom-right:* Illustration of almost periodic and strongly modulated response regimes.

dissipation in the contact region [7, 8, 9, 10, 11, 12, 13], and thus acts as vibro-impact NES[1]. In contrast, the IES relies on the energy transfer (scattering) to and dissipation by high-frequency modes (yielding IMTET); more specifically, the collisions induce elasto-dynamic waves within the host structure and thus transfer energy from the critical low-frequency system modes to high-frequency ones (*energy scattering* or *dispersion effect*). Momentarily assuming for simplicity the same inherent damping ratio for all modes, high-frequency modes dissipate energy more rapidly as they accumulate more vibration cycles within a given time span. Thus, the host structure's inherent damping (due to, e. g., friction joints, distributed material and aerodynamic damping) is exploited more efficiently than in the case without IES. In this sense, the IES helps the structure to damp itself, i. e. to activate its own (inherent) dissipative capacity. This working principle was theoretically analyzed for systems under impulsive/shock loading in [17, 3, 4], and for resonantly-driven vibrations in [2, 5, 6]. In the case of the ID, the local material dissipation is typically associated with inelastic deformation and damage. This might not be a critical point for shock mitigation, where damage accumulates only sporadically, but it can be an important technical limitation for the case of sustained external or self-excitation. The IES and its casing can be designed to avoid the concentration of plastic behavior in the contact region, which is believed to be crucial from an engineering perspective. Moreover, the system behavior can be much better predicted (since empirical laws to describe the local contact dissipation and plastic damage are not necessary).

Although the IES does not rely on local dissipation, and thus does not fall into the category of the NES, it shares many of its characteristics, including the limited amplitude range and the typical vibration regimes. The limited amplitude range is illustrated in Fig. 1-right for the case of resonant excitation. At low excitation level, no or seldom impacts occur so that the system responds as if the absorber was not present. At high excitation level, the clearance becomes negligible compared to the vibration amplitude so that the absorber just adds mass. Between these extreme cases of low and high excitation levels, the resonant response can be considerably reduced compared to the case without absorber. Two regimes of steady-state response are typical for resonantly-driven host structures with a NES/IES: an almost periodic response where the NES/IES and the host structure oscillate in a synchronized way (1:1 resonance), and a strongly modulated response with repeated so called transient resonance captures, where phases with synchronous

[1]The name Vibro-Impact Nonlinear Energy Sink (VI-NES) is now frequently used for the impact damper [1, 14, 15]. Apparently, the impact damper dates back to the 1930s [16]. In contrast, the concept of the NES and the theoretical framework for its analysis was only recently proposed [1].

Journal Pre-proof

Journal Pre-proof

oscillation alternate with phases with almost inactive NES/IES [1]. Depending on the excitation level, the resonant response occurs in either the almost periodic or the strongly modulated range. Interestingly, the point of optimum performance (minimum resonant response) coincides in good approximation with the transition point: For slightly higher excitation level, the resonant response is almost periodic, while for slightly lower excitation level, the resonant response is strongly modulated [18]. For a harmonically driven single-degree-of-freedom host structure, it was shown by Gendelman [19] that a sufficiently light absorber synchronizes with the movement of the cavity walls for appropriate amplitude-to-clearance ratios, independent of the frequency. In the present work, a many-degree-of-freedom structure is considered, and the hypothesis is formulated that synchronization occurs with the displacement-dominant mode (if one exists), regardless of the excitation.

A NES/IES has no preferential frequency and can engage into resonance with arbitrary modes of the host structure. This is an important benefit over the classical tuned vibration absorbers, such as the linear tuned-mass damper [20], the nonlinear tuned vibration absorber [21], or the Stockbridge damper [22, 23, 24]. The strong TET via transient resonance captures is also an important distinction between impact and particle dampers. In spite of the somewhat similar setup, particle dampers mainly introduce local dissipation (inelastic deformation, dry/fluid friction) [25], with the aforementioned detrimental effects on service life, and TET does not play any important role. The ability to engage into resonance with arbitrary modes is the reason why the impact absorber is generally believed to have broadband efficacy. Here, *broadband efficacy* refers to the ability of a properly designed device to substantially reduce the response level of a large number of modes, spanning a wide range of natural frequencies. However, this belief is not well-supported and it is the purpose of the present work to analyze its limitations. The great majority of research has focused on host structures that can be properly described with a single degree of freedom. And those works that consider a continuous / multi-modal structure have mostly focused on the mitigation of the fundamental mode. To the best of the authors' knowledge, only Chabrier et al. [26] so far studied the mitigation of the next few higher modes (with an emphasis on modes 2 to 4; parts of the analysis go to mode 10). They found that the effectiveness of the impact absorber is considerably decreased for higher mode orders under harmonic near-resonant excitation. Similarly, under broadband random excitation, mainly the displacement level of the fundamental mode was reduced. The physical reasons for those observations are so far unknown.

In the present work, the broadband efficacy of the impact absorber is analyzed theoretically/computationally. Two excitation scenarios are considered, namely harmonic forcing, near the resonance with the fundamental and high-order modes, and random forcing, whose effective bandwidth spans multiple high-order natural frequencies. Besides the mitigation of the displacement level, also the performance for mitigating stresses is investigated. As host structure, a taut string is considered; the problem setting, its technical motivation, and the computational approach are described in Section 2. The results for harmonic and random forcing are presented in Section 3 and Section 4, respectively. The goal of the analysis is to achieve a deep understanding of the synchronization and IMTET responsible for the observed phenomena. This article ends with concluding remarks in Section 5.

2. Problem setting and simulation

The problem setting is illustrated in Fig. 2. It consists of a pinned-pinned taut string, with a single impact absorber, under uniformly distributed external forcing ($f(t)$). Ideally, taut strings have equally spaced natural frequencies, so that a random forcing with an effective bandwidth in the order of, e. g., 5 % to 25 % is likely to span multiple modes, if the spectrum is centered around a sufficiently high frequency. This is in complete contrast to, e. g., beams, as their natural frequencies are much more widely spaced. The relatively close spacing of natural frequencies, compared to beams for instance, seems ideal for the purpose of the present study, because intense IMTET can therefore be expected.

The model of the taut string is updated in accordance with an existing test rig, as described in Appendix B. A base piano string of 1 m length was pinned at both ends and taut using dead weights. Initially, experiments with an impact absorber were planned. This idea was abandoned in view of the relatively poor performance found in the simulations. Compared to a completely generic taut string model, the updated model has the important benefit that well-supported modal damping values can be used, which are expected to have a crucial effect on the modal energy distribution. Besides the modal damping ratios, the bending stiffness and the rotational inertia due to the clamping are identified, both of which turned out to have an important effect on the higher-frequency modes.

An important technical motivation for considering a taut string as host structure is the vortex-induced vibrations of

Journal Pre-proof

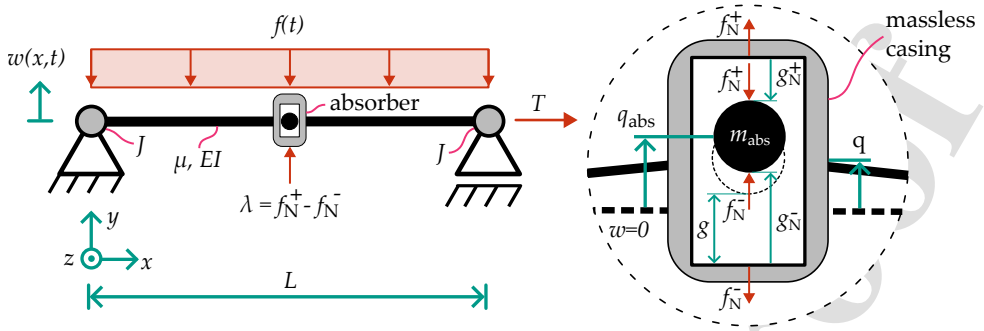

Figure 2: Illustration of the problem setting.

overhead transmission lines and stay cables [27, 28, 29]. For sufficiently small wind speeds, the flow is laminar, and the vortex shedding typically leads to self-excited vibrations. The effect of NESs on such vibrations is analyzed, e. g., in [30, 31]. For sufficiently high wind speeds, the flow is turbulent, and the vortex shedding is better characterized as stationary random external forcing. This type of excitation is known to be responsible for fatigue problems. The power spectral density is commonly described as Gaussian-bell-curve (Vickery-Clark model [32]). The central frequency is a function of wind speed, characteristic length and Strouhal number (dependent on cross section geometry). There is evidence for a substantial contribution of many high-order modes (about 100) to measured vibrations of stay cables [29]. Vortex-induced vibrations of transmission lines / cables serve as motivating technical application for the present work. Consequently, the stationary random excitation is also assumed in the form of a Gaussian-bell-type power spectral density, centered around a high-order mode.

2.1. *Equations of motion*

The transversal displacement $w(x,t)$ of the taut string is governed by the equations:

$$\mu\frac{\partial^2 w}{\partial t^2} - T\frac{\partial^2 w}{\partial x^2} + EI\frac{\partial^4 w}{\partial x^4} = -f(t) + \delta(x - x_{\text{abs}})\,\lambda\,, \tag{1}$$

$$w(0,t) = 0\,, \tag{2}$$

$$w(L,t) = 0\,, \tag{3}$$

$$\left[EI\frac{\partial^2 w}{\partial x^2} - J\frac{\partial^3 w}{\partial^2 t\,\partial x}\right]_{x=0,t} = 0\,, \tag{4}$$

$$\left[EI\frac{\partial^2 w}{\partial x^2} + J\frac{\partial^3 w}{\partial^2 t\,\partial x}\right]_{x=L,t} = 0\,. \tag{5}$$

Herein, the partial differential equation (1) is defined in the domain of the span-wise coordinate $x \in (0,L)$ and time $t \in \mathbb{R}$. $\mu > 0$, $T \geq 0$ and $EI > 0$ are lineic mass, tensile force and bending stiffness; the relevant area moment of inertia is $I = I_{zz} > 0$, and J is the rotational inertia associated with the clamping. As the bending stiffness is non-negligible, the structure is a pre-stressed beam; as a piano string was actually used in the test rig, the term taut string is preferred. Note that the uniform loading $f(t)$ is in negative y-direction. $\delta(\xi)$ is the Dirac-delta-distribution. The absorber is placed at the center ($x_{\text{abs}} = L/2$) if not stated otherwise. Finally, λ is the interaction force between absorber and string. The absorber consists of a spherical mass, m_{abs}, placed into a casing (assumed to have negligible mass). The displacement, with respect to the inertial frame of reference, of the absorber mass is denoted as q_{abs}, and that of the casing as q (Fig. 2-right). The static force balance at the casing, Eq. (6), and the impulse balance at the absorber mass, Eq. (7), can be expressed as

$$f_{\text{N}}^{+} - f_{\text{N}}^{-} - \lambda = 0\,, \tag{6}$$

$$m_{\text{abs}}\ddot{q}_{\text{abs}} + f_{\text{N}}^{+} - f_{\text{N}}^{-} = 0\,, \tag{7}$$

Journal Pre-proof

where $f_{\mathrm{N}}^{\pm}$ are the contact forces between absorber mass and casing, as indicated in Fig. 2-right. Throughout this work, the absorber mass m_{abs} is set to 4 % of the string mass (μL). As shown in [33, 6], for nominal point contacts between smooth metallic surfaces, plasticity causes the formation of a small crater during the first few impacts, beyond which elastic behavior holds in very good approximation. The contact is then well described by the Hertzian contact law

$$f_{\mathrm{N}}^{\pm}\left(g_{\mathrm{N}}^{\pm}\right) = \begin{cases} k_{\mathrm{N}}\left|g_{\mathrm{N}}^{\pm}\right|^{3/2} & \text{if } g_{\mathrm{N}}^{\pm} < 0 \\ 0 & \text{otherwise} \end{cases}, \tag{8}$$

$$g_{\mathrm{N}}^{+} = g-(q_{\mathrm{abs}}-q)\,, \tag{9}$$

$$g_{\mathrm{N}}^{-} = g+(q_{\mathrm{abs}}-q)\,, \tag{10}$$

$$k_{\mathrm{N}} = \frac{4}{3}\sqrt{R}E^{*}\,. \tag{11}$$

The casing is assumed as rigidly attached to the string, so that $q(t) = w(x_{\mathrm{abs}},t)$. g is the clearance when $q_{\mathrm{abs}} = q$. The Hertzian spring constant depends, as specified in Eq. (11), on the effective elastic modulus E^{*} and the effective contact radius R. The value is set to $k_{\mathrm{N}} = 1.8676\cdot 10^{10}\,\mathrm{N/m^{3/2}}$, which is in the order of magnitude as that identified in [6]. The conservative character of the contact law excludes ongoing immediate dissipation in the contact region. Again, this is in line with the experimental findings in [33, 6], and permits an extensive use of IMTET.
The model of the string is truncated to the M lowest-frequency mass-normalized mode shapes (without absorber), $\varphi_k(x/L)$,

$$w(x,t) = \sum_{k=1}^{M}\varphi_k(x/L)\eta_k(t)\,. \tag{12}$$

The computation of the mode shapes and modal frequencies is described in Appendix A. Substitution into Eq. (1) and requiring that the residual is orthogonal to the retained modes (Galerkin projection; classical modal truncation), yields the set of ordinary differential equations

$$\ddot{\eta}_k + 2D_k\omega_k\dot{\eta}_k + \omega_k^2\eta_k - \varphi_{q,k}\left(f_{\mathrm{N}}^{+}-f_{\mathrm{N}}^{-}\right) = \varphi_{f,k}f(t) \quad k=1,\ldots,M\,. \tag{13}$$

Herein, Eq. (6) was used. ω_k and $D_k > 0$ are the angular frequency and the damping ratio of mode k. $\varphi_{q,k} = \varphi_k(x_{\mathrm{abs}}/L)$ and $\varphi_{f,k} = -L\int_0^1\varphi_k(\xi)\mathrm{d}\xi$. Only symmetric configurations of the mechanical system and its excitation are considered. Consequently, it holds that $\varphi_{q,k} = 0$ and $\varphi_{f,k} = 0$ for the even-ordered modes ($k = 2,4,\ldots$), leaving the trivial steady-state response ($\eta_k = 0$) as the only solution of Eq. (13) for those modes. Thus, Eq. (13) and Eq. (12) are truncated to the odd-ordered modes ($k = 1,3,\ldots$).

k	1	3	5	7	9	11	13	15	17	19	21	23	25
D_k in %	0.75	0.96	1.15	1.13	1.17	1.15	0.90	0.61	0.40	0.33	0.31	0.33	0.30
$\frac{\omega_k}{2\pi}$ in Hz	12.5	38.3	66.2	97.4	133	173	220	272	330	394	465	542	625
	27	29	31	33	35	37	39	41	43	45	47	49	>49
	0.25	0.68	0.35	0.30	0.08	0.21	0.22	0.24	0.16	0.25	0.47	0.38	0.2
	714	809	910	1016	1128	1246	1370	1500	1639	1784	1937	2098	-

μ	L	T	EI	J	x_{abs}/L	$m_{\mathrm{abs}}/(\mu L)$	k_{N}
$0.3288\,\frac{\mathrm{kg}}{\mathrm{m}}$	1 m	205.03 N	$0.1033\,\mathrm{Nm^2}$	$2.6257\cdot 10^{-7}\,\mathrm{kgm^2}$	0.5	0.04	$1.8676\cdot 10^{10}\,\mathrm{Nm^{-3/2}}$

Table 1: Specified and experimentally identified system parameters.

The parameters of the string (L, μ, T, EI, J, D_k) were identified from an existing test rig as described in Appendix B, and listed in Tab. 1. The parameters of the absorber (x_{abs}/L, $m_{\mathrm{abs}}/(\mu L)$, k_{N}) were selected as specified above and

Journal Pre-proof

are also listed in Tab. 1 for convenience. The clearance g is the key parameter that was varied in a wide range, as explained in Section 3 and Section 4. Also, the parameters of the forcing are defined later for the different excitation scenarios.

2.2. Numerical solution; excitation scenarios; quantities of interest

For a given forcing $f(t)$, Eqs. (13) and (7), under consideration of Eqs. (8)-(10), are simulated using numerical time step integration. Due to the high contact stiffness and the large range of relevant natural frequencies, the problem is numerically stiff. The explicit third-order Bogacki-Shampine scheme is used, which is well-suited for this case. As mentioned before, two excitation scenarios are considered: harmonic and random forcing. In any case, the simulation starts from homogeneous initial conditions. The only exception is the absorber, which is placed close to a wall ($q_{\mathrm{abs}}(0) = 0.99g$), as it was observed that this shortens the transient. The simulation is then carried out until the transients have decayed, and a steady-state time interval is available that is sufficiently long to achieve convergence among the quantities of interest, as specified later per excitation scenario.

2.2.1. Excitation scenarios

For the case of harmonic excitation, the forcing is

$$f(t) = \sqrt{2} f_{\mathrm{RMS}} \cos(\Omega t)\,, \tag{14}$$

with the constant amplitude $\sqrt{2} f_{\mathrm{RMS}}$ and the angular frequency Ω. Throughout this work, $f_{\mathrm{RMS}} = 12.9\ \mathrm{N/m}$ was used. A focus was placed on the primary resonance with the fundamental mode ($\Omega \approx \omega_1$) and a high-order mode ($\Omega \approx \omega_{35}$). Due to the nonlinear behavior, the exact location of the resonance, in terms of the maximum response level, is not a priori known. To determine this, and to robustly ensure steady-state results, the stepped sine procedure proposed in [6] was adopted.

For the case of random excitation, $f(t)$ is assumed as stationary Gaussian process with the power spectral density

$$S_{ff}(\Omega) = \begin{cases} \frac{f_{\mathrm{RMS}}^2}{\Omega_{\mathrm{c}} B \sqrt{\pi}} \mathrm{e}^{-\left(\frac{\Omega-\Omega_{\mathrm{c}}}{B\Omega_{\mathrm{c}}}\right)^2} & \text{if} \quad \Omega_{\min} \le \Omega \le \Omega_{\max} \\ 0 & \text{otherwise} \end{cases}. \tag{15}$$

The root-mean-square value f_{RMS} was set as in the case of harmonic forcing. The central frequency was set to $\Omega_{\mathrm{c}} = 1058.2$ Hz and the bandwidth parameter was set to $B = 0.4$. In this way, the modes 29 to 37 are in the half-power bandwidth. Eq. (15) corresponds to the Vickery-Clark model [32]; it should be remarked, however, that more narrow bandwidths, $B \in [0.08; 0.3]$, are typically reported for the case vortex-induced vibrations of stay cables and transmission lines, but the number of modes in the half-power bandwidth is representative for this application [29]. Also, it should be remarked that vortex-induced vibrations of large structures do not cause (fully) coherent loading, in contrast to what is assumed in the present work. A more coherent loading leads to a more pronounced excitation of the lower-order modes.

2.2.2. Stochastic simulation

For the stochastic simulation, individual (discrete) time series of $f(t)$ are generated using the Monte-Carlo algorithm proposed in [34], which is based on a spectral decomposition of S_{ff} [35]. The truncation of the spectrum by the lower bound $\Omega_{\min} > 0$ and the upper bound $\Omega_{\max} < \infty$ is needed to achieve a finite simulation time and a finite time discretization, respectively. In addition, a tighter truncation to only the half-power bandwidth, i. e., $\Omega_{\mathrm{c}} \pm 23.6\%$, is used in one case in order to further reduce the excitation of the low-frequency modes.

It is crucial to reach sufficient convergence among the quantities of interest. To ensure sufficiently steady state behavior and exclude transient effects, the first $t_{\mathrm{tr}} = 11.72$ s of the simulation were scraped; this corresponds to the time it takes to decrease the homogeneous solution of the underlying linear autonomous system down to 0.1%. Here, the slowest decay rate is relevant, i. e., $t_{\mathrm{tr}} = \ln(1000)/(D_1 \omega_1)$. A total simulation time of $t_{\mathrm{sim}} = 150$ s (including t_{tr}) was found appropriate to reach sufficient statistical convergence. Moreover, 25 stochastic simulations are carried out, and the mean is depicted along with the corrected sample standard deviation.

Journal Pre-proof

Based on a modal convergence study, a truncation order of $M = 221$ was selected.[2] Given that the highest mode in the effective excitation bandwidth is $k = 37$, this value seems quite large. This is explained by the facts that, first, the impacts scatter a substantial portion of the energy to high-frequency modes and, second, the high-order modes are particularly important for the convergence of the stress level (one of the quantities of interest). Based on a time step convergence study, the shortest modal period was divided into 20 levels, i. e. $\Delta t = (2\pi/\omega_{221})/20 = 2.529 \cdot 10^{-6}$ s. This leads to 130 million time levels for a single simulation (t_{sim}). Thus, one might notice that the problem is computationally somewhat demanding [3].

2.2.3. Quantities of interest

The quantities of primary interest are the transversal displacement and the dynamic stress in the string. These are evaluated at the center ($x = L/2$),

$$q(t) = w(L/2,t), \tag{16}$$

$$\sigma(t) = |y|_{\max} E \underbrace{\left.\frac{\partial^2 w}{\partial x^2}\right|_{x=L/2,t}}_{=c(t)}. \tag{17}$$

Herein, c denotes the curvature evaluated at the center. Eq. (17) assumes a uniform cross section, which is questionable for the given test rig, see previous footnote. Also, besides the dynamic stress, other measures could be of relevance in practice to describe fretting fatigue, for instance. In any case, $\sigma(t)$, as defined in Eq. (17), is considered as qualified indicator for damage/structural integrity. It should also be noted that only normalized stress values, divided by the linear reference, are used in this work. At the center, all (relevant, i. e., odd-ordered) modes have an anti-node, which leads to the largest displacements. Under the described random excitation, the curvature (and thus the stress) level obtained in the case without absorber also has a local maximum there (Fig. 3). In the case of ideal boundary conditions, this is also the global maximum. The non-ideal boundary conditions (finite rotational inertia $J > 0$) cause a boundary maximum of the stress, which is almost of equal height as the maximum at the center. Another reason why the stress should be evaluated at the center is that the concentrated absorber-string interaction force introduces local stress there. The quantities of interest were evaluated at different locations, including the center and the boundary; the results obtained at the center were found to be representative and thus only these are shown.

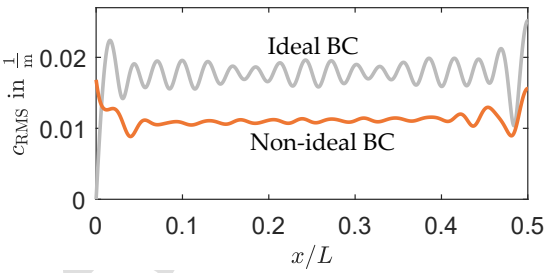

Figure 3: Curvature level c_{RMS} vs. x/L in the symmetric half of the string (without absorber) under broadband excitation.

[2] It should be remarked here that Euler-Bernoulli theory becomes inaccurate when the dimensions of the wave length of the mode shapes become shorter than 10 times the string's diameter of $d = 10$ mm. For modes $k = 35$ and $k = 221$, the ratios between their wavelength l_k and the diameter d are $l_{35}/d = 5.7$ and $l_{221}/d = 0.9$. A good agreement with the tested string can therefore not be expected for mode orders $k \geq 35$. For a homogeneous cross section area, Timoshenko theory provides higher accuracy than Euler-Bernoulli theory. However, due to the setup of the tested string (steel core with double copper winding), the cross section is far from being homogeneous. Hence, no significant improvement is expected from using Timoshenko theory. Finally, it should be emphasized that the purpose of the model updating is not a perfect agreement with the tested string, but to find representative parameters of a real system (in particular for the damping).

[3] On our system (Intel i9-10980XE CPU@3.00GHz and MATLAB Simulink R2020b), a single simulation takes around 30 minutes to complete.

Journal Pre-proof

As a measure for displacement and stress level, the respective root-mean-square values is used, q_{RMS}, σ_{RMS},

$$q_{\mathrm{RMS}} = \sqrt{\frac{1}{t_{\mathrm{sim}}-t_{\mathrm{tr}}}\int_{t_{\mathrm{tr}}}^{t_{\mathrm{sim}}} q^2(t)\mathrm{d}t}\,, \tag{18}$$

$$\sigma_{\mathrm{RMS}} = \sqrt{\frac{1}{t_{\mathrm{sim}}-t_{\mathrm{tr}}}\int_{t_{\mathrm{tr}}}^{t_{\mathrm{sim}}} \sigma^2(t)\mathrm{d}t}\,. \tag{19}$$

These are easy to evaluate from a given time series. To analyze their frequency content, the power spectral densities of q and σ, S_{qq} and $S_{\sigma\sigma}$, are also determined. These are estimated using Welch's method. More specifically, the steady-state time section is divided into 8 segments with 50 % overlap and a Hamming window is used for each segment (default settings of MATLAB's function 'pwelch'). To directly analyze the IMTET, the time-averaged modal energies are also useful:

$$E^{\mathrm{mod}}_{\mathrm{avg},k} = \frac{1}{t_{\mathrm{sim}}-t_{\mathrm{tr}}}\int_{t_{\mathrm{tr}}}^{t_{\mathrm{sim}}} \frac{1}{2}\dot{\eta}_k^2 + \frac{1}{2}\omega_k^2\eta_k^2\mathrm{d}t \tag{20}$$

$$= \frac{1}{2}\dot{\eta}^2_{k,\mathrm{RMS}} + \frac{1}{2}\omega_k^2\eta^2_{k,\mathrm{RMS}}\,. \tag{21}$$

For the last step, the definition of the root-mean-square value is used (cf.Eqs. (18)-(19)). The modal energies will be depicted in a normalized way, scaled by the total energy in the string, $E^{\mathrm{tot}}_{\mathrm{avg}} = \sum_{k=1}^{M} E^{\mathrm{mod}}_{\mathrm{avg},k}$.

2.3. Analytical expression of quantities of interest in the linear reference case

The linear configuration of the string alone (without absorber) will serve as reference. For this case, the power spectral densities S_{qq} and $S_{\sigma\sigma}$ can be expressed in closed form:

$$S_{qq} = \left|G_{qf}\right|^2 S_{ff}\,, \tag{22}$$

$$S_{\sigma\sigma} = \left|G_{\sigma f}\right|^2 S_{ff}\,, \tag{23}$$

$$G_{qf} = \sum_{k=1}^{M} \underbrace{\frac{\varphi_{q,k}\varphi_{f,k}}{-\Omega^2+2D_k\omega_k\mathrm{i}\Omega+\omega_k^2}}_{g_{qf,k}}\,, \tag{24}$$

$$G_{\sigma f} = \sum_{k=1}^{M} \underbrace{\frac{\varphi_{\sigma,k}\varphi_{f,k}}{-\Omega^2+2D_k\omega_k\mathrm{i}\Omega+\omega_k^2}}_{g_{\sigma f,k}}\,. \tag{25}$$

Herein, $\varphi_{f,k}$ is as defined below Eq. (13), $\varphi_{q,k} = \varphi_k(1/2)$, and $\varphi_{\sigma,k} = |y|_{\max} E/L^2\varphi_k''(1/2)$. The denominator in Eq. (24) and Eq. (25), $-\Omega^2+2D_k\omega_k\mathrm{i}\Omega+\omega_k^2$, corresponds to the dynamic modal stiffness. As explained above, only the odd-ordered modes are considered within the sums in Eqs. (24)-(25).
For an ergodic process, the root-mean-square value of the quantity q is related to the power spectral density S_{qq} through Parseval's theorem

$$q_{\mathrm{RMS}} = \sqrt{\int_{\Omega_{\min}}^{\Omega_{\max}} S_{qq}\mathrm{d}\Omega}\,. \tag{26}$$

The analog of this holds for the relation between σ_{RMS} and $S_{\sigma\sigma}$.

Journal Pre-proof

3. Harmonic excitation

3.1. Resonance with mode 1

First, the commonly studied case is considered, where harmonic forcing with a frequency near the fundamental natural frequency is applied. Of primary interest is the highest response level reached in the frequency band near the linear natural frequency (*resonant response level*). Due to the nonlinear character of the system, the highest response level does not necessarily occur exactly at the linear natural frequency. Typically, the resonant response occurs at frequencies (slightly) smaller than in the linear reference case without absorber, since the absorber effectively adds mass. As mentiond before, the method proposed in [6] was adopted to determine the resonant response level, which involves a sufficiently fine forward/backward sine stepping procedure. The clearance g is a key parameter of the impact absorber, and it was varied in a wide range.

The resonant displacement level, q_{RMS} is depicted in Fig. 4a vs. g. Recall that *reference* refers to the case without

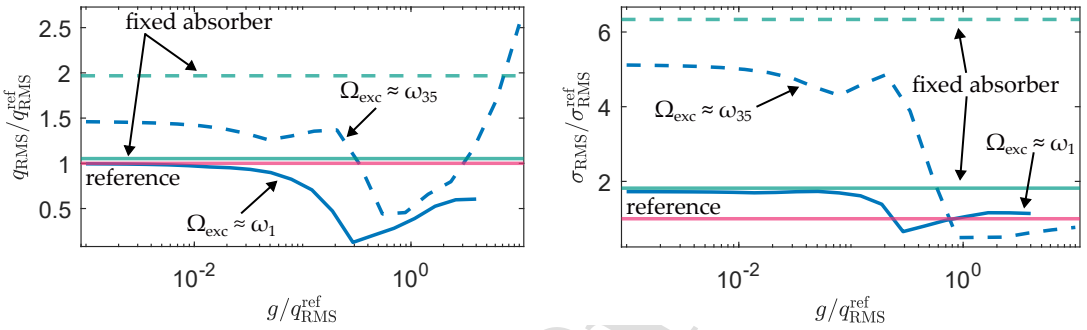

Figure 4: Resonant response level vs. clearance under harmonic forcing: (a) displacement level q_{RMS} and (b) stress level σ_{RMS}. The solid lines refer to the primary resonance with the fundamental mode ($\Omega_{\mathrm{exc}} \approx \omega_1$) and the dashed lines to that with the 35-th mode ($\Omega_{\mathrm{exc}} \approx \omega_{35}$). The horizontal lines denote the respective linear limit cases of no (red) and fixed (green) absorber. $q_{\mathrm{RMS}}^{\mathrm{ref}}$ and $\sigma_{\mathrm{RMS}}^{\mathrm{ref}}$ are different for both cases of Ω_{exc}.

absorber; the other linear limit case with fixed absorber is also indicated. For small clearance, the system behavior resembles that of the string with fixed absorber. For large clearance, it resembles that of the string without absorber. Between these limit cases, the displacement level is reduced down to 13% of the reference (no absorber). This confirms the high efficacy of the impact absorber for mitigating resonances with the fundamental mode. The extent of the mitigation effect is in the range expected from the available literature on continuous / multi-modal structures [36, 37, 38, 39, 40, 41, 42, 43, 44, 26, 6]. It was ascertained that, even though the mitigation is caused by scattering to high-frequency modes, the displacement response is still dominated by the fundamental mode; i. e., the fundamental mode is the *displacement-dominant mode*. More specifically, in the linear case, almost 100 % of q_{RMS} are caused by the fundamental (resonant) mode. Also as expected, it was observed that at / near $g = g_{\mathrm{opt}}$ the critical response regime changes from an almost periodic response with two symmetric impact per period to a strongly modulated response. Here and in the following, g_{opt} denotes the clearance that leads to the minimum displacement level and can be found at $g_{\mathrm{opt}}/q_{\mathrm{RMS}}^{\mathrm{ref}} = 0.29$ for the resonant harmonic excitation of the fundamental mode.

The resonant stress level, σ_{RMS}, is depicted in Fig. 4b. For small and large clearance, the corresponding linear limit cases are again reached. Interestingly, the stress level is doubled when the absorber is rigidly attached, compared to the case without absorber. The corresponding effect on the displacement level is almost negligible. Apparently, the increased stress level is caused by the attached mass, which induces a concentrated inertia load ($m_{\mathrm{abs}}\ddot{q}$). When the mass is left free to undergo impacts, there are counteracting effects on the stress level: First, the mass is temporarily attached during the contact phases, which increases the stress due to concentrated inertia loading. Second, the impacts scatter energy from the resonant fundamental to high-frequency modes, which should increase the stress, because the stress induced by a certain mode increases with its mode order (for the same amount of energy), as shown in Appendix A. Finally, as the scattering is almost irreversible, energy is removed from the fundamental mode, which decreases the overall power input to the system, thus reducing the stress level. Apparently, the last mechanism (slightly) dominates,

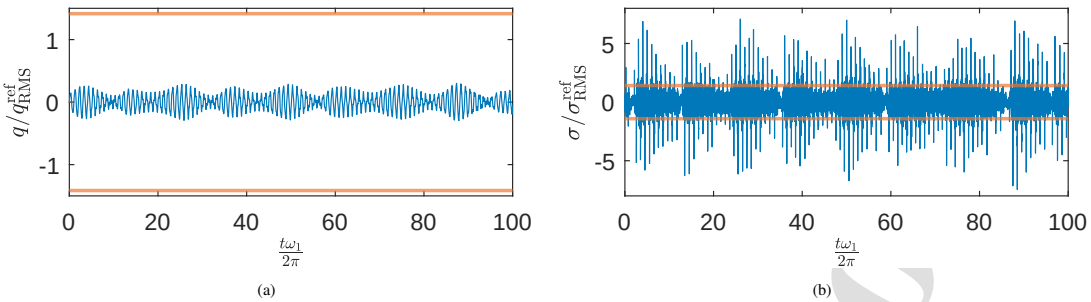

Figure 5: Typical resonant response under harmonic excitation near the fundamental mode for $g = g_{\mathrm{opt}}$: (a) Displacement and (b) stress. The horizontal lines indicate the linear reference amplitude.

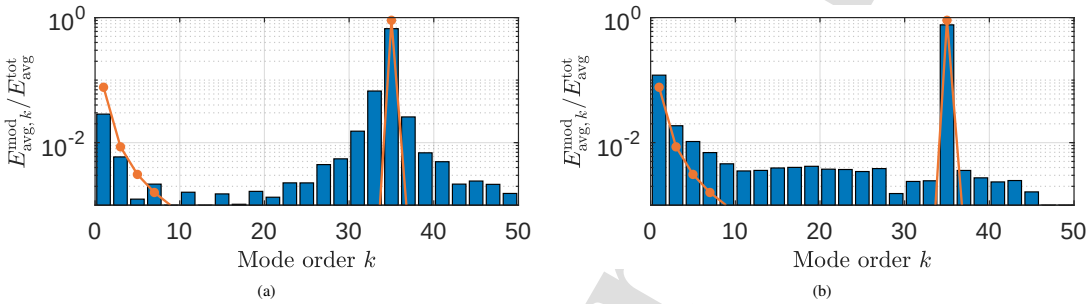

Figure 6: Modal energy distribution in the taut string under harmonic excitation near mode 35: (a) $g = g_{\mathrm{opt}}$ and (b) $g = 10 \cdot q_{\mathrm{RMS}}^{\mathrm{ref}}$. Blue: System with absorber. Orange: reference system (without absorber). Both systems are normalized with their respective $E_{\mathrm{avg}}^{\mathrm{tot}}$.

so that the stress level is reduced to 80% for the optimum clearance setting, $g = g_{\mathrm{opt}}$. While the stress level, in terms of the root-mean-square value, is reduced, however, the impacts induce stress spikes (Fig. 5b) that exceed the linear reference by more than factor five.

3.2. Resonance with mode 35

Next, the resonance with mode 35 is analyzed. The results are also shown in Fig. 4 (dashed lines). The qualitative behavior is the same. In this case, both displacement and stress level are reduced by ca. factor two.
To better interpret the results, the modal energy distribution is depicted in Fig. 6 for the optimum and a much larger clearance. Apparently, not only mode 35 but also the fundamental (and the next few) modes contribute significantly to the vibration, both in the linear and in the nonlinear case. If the modal basis is truncated to only mode $k = 35$, one would obtain $0.95 \cdot q_{\mathrm{RMS}}(M = 221)$ in the linear reference case. Truncating to the fundamental mode, i. e. setting $M = 1$, however, still results in $0.39 \cdot q_{\mathrm{RMS}}(M = 221)$.
The pronounced contribution of low-order modes may seem surprising at first and shall be made plausible in the following for the case of an ideal taut string (without absorber). In the linear case, we have

$$\hat{q} = \sum_{k=1}^{M} \varphi_{q,k} \hat{\eta}_k = \sum_{k=1}^{M} g_{qf,k} \hat{f}\,, \tag{27}$$

where $g_{qf,k}$ is defined in Eq. (24). For an ideal taut string ($J = 0 = EI$), $|\varphi_{q,k}| = \text{const}$ and $\varphi_{f,k} \sim 1/k$ (for the considered uniform forcing, see Appendix A). The dynamic stiffness of the off-resonant low-order modes ($\ell = 1$ and the next few) is dominated by Ω^2 since $\Omega \gg \omega_\ell$ for these modes. For light damping, the dynamic stiffness of a resonant mode ($\Omega = \omega_k$) is $2D_k\omega_k^2\mathrm{i}$. Thus, the ratio between the off-resonant contribution of low-order mode ($\ell \approx 1$)

Journal Pre-proof

and a resonant high-order mode ($k \approx 35$) to the displacement q is

$$\frac{\varphi_{q,\ell}\,|\hat{\eta}_\ell|}{\varphi_{q,k}\,|\hat{\eta}_k|} = \frac{\left|g_{qf,\ell}\right|}{\left|g_{qf,k}\right|}, \tag{28}$$

$$\approx \frac{\varphi_{f,\ell}\varphi_{q,\ell}}{\varphi_{f,k}\varphi_{q,k}}\frac{2D_k\omega_k^2}{\omega_k^2}, \tag{29}$$

$$\approx 2D_k\frac{k}{\ell}. \tag{30}$$

With respect to the fundamental mode, $\ell = 1$, we obtain $2D_{35}\cdot 35 = 0.056$ and $2D_{33}\cdot 33 = 0.198$, using the damping ratios listed in Tab. 1. Thus, the low-order modes contribute non-negligibly to the displacement.
The energy ratio between mode 1 and mode 35 at the resonance $\Omega = \omega_{35}$ is

$$\frac{E_1^{\mathrm{mod}}}{E_{35}^{\mathrm{mod}}} = \frac{\frac{1}{2}\omega_1^2|\hat{\eta}_1|^2 + \frac{1}{2}\omega_{35}^2|\hat{\eta}_1|^2}{\omega_{35}^2|\hat{\eta}_{35}|^2}, \tag{31}$$

$$= \frac{1}{2}\frac{\omega_1^2+\omega_{35}^2}{\omega_{35}^2}\left|\frac{\varphi_{q,1}\varphi_{f,1}}{\varphi_{q,35}\varphi_{f,35}}\right|^2 \frac{\left(2D_{35}\omega_{35}^2\right)^2}{\left(\omega_1^2-\omega_{35}^2\right)^2+\left(2D_1\omega_1\omega_{35}\right)^2}, \tag{32}$$

$$\approx 2\cdot 35^2\cdot D_{35}^2 \backsimeq 0.16\,\%. \tag{33}$$

For the last step, it was exploited that $\varphi_{f,k}\sim 1/k$, $\left|\varphi_{q,1}\right| = \left|\varphi_{q,35}\right|$, $\omega_{35}^2 \gg \omega_1^2$, so that the super-critical contribution of the dynamic stiffness of mode 1 is dominated by the modal inertia forces. It must be noted that these approximations even underestimate the influence of the fundamental mode of the system with finite rotational inertia and bending stiffness $EI, J > 0$. This is mainly caused by the more complicated behavior of $\varphi_{f,k}$ and $\varphi_{f,k}$ as indicated in Fig. A.14. At (and near) the optimum clearance g_{opt}, the IMTET leads to a reduction of the energy of the resonant high-order and the low-order modes $\ell = 1,\ldots,9$. In contrast, the energy in the intermediate and the high-order off-resonant modes is increased. This leads to an overall reduced displacement and stress level. The stress-optimal clearance is slightly larger (Fig. 4). If the impacts were synchronized with a high-frequency mode, e. g. mode 35, it would be expected that the action on the low-frequency modes would average out. However, for clearances larger than $g_{\mathrm{opt}}/q_{\mathrm{RMS}}^{\mathrm{ref}} = 0.55$, the critical regime is a strongly modulated response, where the impacts are not synchronized with a high-frequency mode but occur less frequently and in an irregular manner. Consequently, energy from the directly driven mode is scattered to lower frequencies, which reduces the stress level. The individual stress spikes were found to only slightly exceed the reference stress level in this case.

4. Random excitation

The harmonic forcing is now replaced by a random forcing with the power spectral density defined in Eq. (15). First, the frequency bounds (Ω_{min}, Ω_{max}) are set in such a way that the band $\Omega_{\mathrm{c}} \pm 99.5\%$ is covered. This will be referred to as *broadband* excitation. In a second case, the frequency bounds are tightened to $\Omega_{\mathrm{c}} \pm 23.6\%$. This will be referred to as *narrow-band* excitation.

4.1. Broadband excitation

The displacement and stress level are depicted in Fig. 7 as function of the clearance. One can see the expected transition between the linear limit cases (small clearance: fixed absorber; large clearance: no absorber / reference). The displacement level is almost the same in both limit cases. In contrast, the stress level is about 2.5 times larger when the absorber is fixed. As in the case of the resonant harmonic excitation, this is explained by the concentrated inertia forces induced by the additional mass of the absorber.
Interestingly, the displacement response under broadband excitation is still dominated by the fundamental mode. This can be observed from the power spectral density depicted in Fig. 8 for the optimum clearance $g_{\mathrm{opt}}/q_{\mathrm{RMS}}^{\mathrm{ref}} = 0.98$. The dashed black curve shows the results for the linear reference obtained when truncating the string to the fundamental mode ($M = 1$). The resonance peaks of the high-order modes do not exceed significantly the S_{qq} obtained for

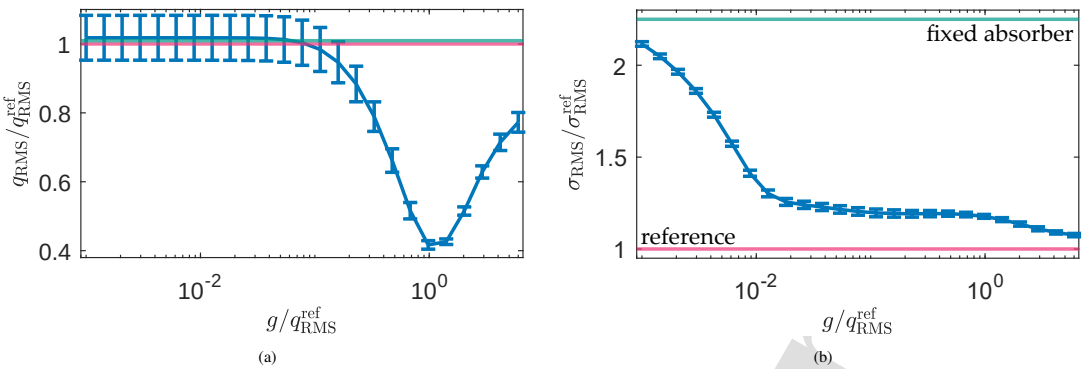

Figure 7: Response level vs. clearance under broadband forcing: (a) displacement level q_{RMS} and (b) stress level σ_{RMS}. The horizontal lines denote the respective linear limit cases of no (red) and fixed (green) absorber.

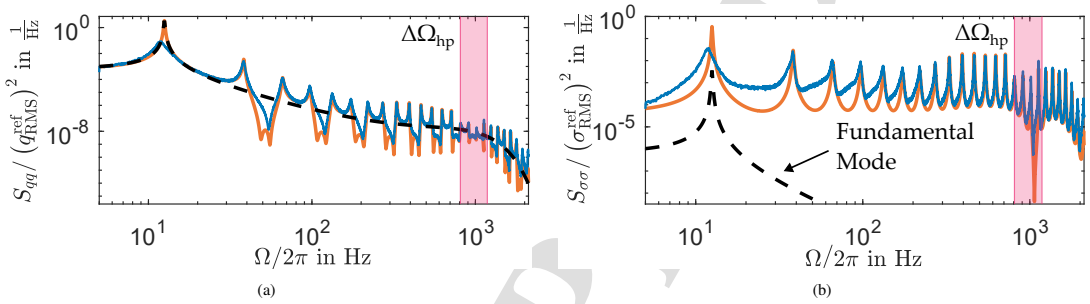

Figure 8: Response power spectral densities for optimum clearance $g = g_{\mathrm{opt}}$ (blue) compared to the reference (orange) under broadband forcing: (a) S_{qq} and (b) $S_{\sigma\sigma}$. The highlighted frequency range depicts the excitation's half-power bandwidth $\Delta\Omega_{\mathrm{hp}}$. The dashed black line shows the response of the linear reference system when the modal basis is truncated to only the fundamental mode.

$M = 1$. The fraction between the resonant contribution of a high-order mode k (i. e. $\Omega = \omega_k$) and the off-resonance contribution of a low-order mode ℓ is given in Eq. (30) (which is a feature of the transfer behavior and hence independent of the type of excitation). Also, there are anti-resonances between the resonances. Because q_{RMS}^2 is the integral of $S_{qq}(\Omega)$ (Eq. (26)), resonances and anti-resonances of high-order modes are somewhat averaged out. Thus, q_{RMS} obtained with $M = 1$ is almost the same as that obtained for the nominal modal truncation order, i. e. $q_{\mathrm{RMS}}(M = 1)/q_{\mathrm{RMS}}(M = 221) = 0.998$.

As the fundamental mode dominates the displacement response, the dynamic behavior has some resemblance with the case of harmonic excitation near the primary resonance with mode 1. This can be shown by the time-averaged number of significant impacts per period of the fundamental linear mode N_{sipp}. For this purpose, a significant impact is defined as an impact between the absorber and the cavity during which the velocity of the absorber changes its sign [45]. For the optimum and slightly smaller clearances (Fig. 9a), the absober synchronizes well with $N_{\mathrm{sipp}} = 1.9$[4], whereas less frequent impacts occur (and with a less regular pattern) in the case of larger clearance (Fig. 9b), yielding only $N_{\mathrm{sipp}} = 1.3$. However, due to the stochastic character of response, there are also time spans of the opposite regime in both cases (of course much more seldom). This can also be seen in the probability density function (PDF) of the time between two consecutive significant impacts Δt_{sipp} in Fig. 9c. For the smaller clearance this is centered around half times the period of the fundamental mode (inidcated by the red line) which is the ideal value for two symmetric significant impacts per period. However, no dominant value can be identified for the clearance larger than g_{opt} (black

[4]Note that it is expected to differ from 2.0 because the reference period corresponds to the resonance frequency of the liner system without absorber; the resonance frequency of the nonlinear system with absorber is typically lower, bringing N_{sipp} closer to 2.0.

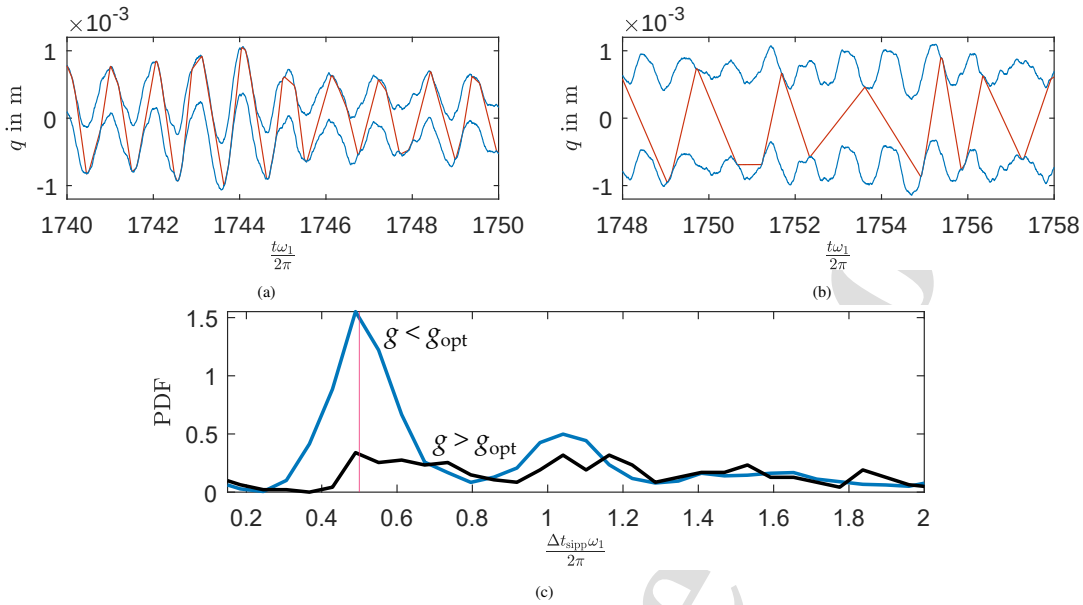

Figure 9: Representative movement of the absorber (red) inside the cavity walls (blue) under broadband excitation for (a) $g < g_{\text{opt}}$, i. e., $g/q^{\text{ref}}_{\text{RMS}} = 0.7 < g_{\text{opt}}$ and (b) $g < g_{\text{opt}}$, i. e., $g/q^{\text{ref}}_{\text{RMS}} = 2.0 > g_{\text{opt}}$ and (c) the PDF of the time between two consecutive significant impacts for both cases indicated by the blue and black line, respectively. The red vertical line indicates the ideal case of two symmetric significant impacts per period.

line). Thanks to the synchronization to the fundamental mode, the absorber effectively mitigates the contribution of this mode. This can be best seen in Fig. 8a. Some energy is scattered to higher modes ($k > 1$); their contribution is not (significantly) reduced. As the response of the displacement-dominant mode is reduced, the overall displacement level is reduced. Because of the stronger contribution of the higher modes, however, the peak performance is less pronounced under broadband excitation, compared to the mono-frequent excitation: The displacement level is reduced to only 40%, compared to the 13% under resonant harmonic excitation. It is believed that the synchronization with a displacement-dominant mode is crucial for the efficacy of the absorber: Only in the synchronized phases of the motion, two significant impacts per (natural) period occur, facilitating strong energy transfers. If the absorber moves at much higher frequency than a given natural frequency, much more frequent impacts occur, whose contribution tends to cancel in average over the natural period. On the other hand, if the absorber moves at much lower frequency, impacts occur only infrequently, also leading to ineffective energy transfer.

The stress level never falls below the reference (Fig. 7b). This is in contrast to the case of harmonic excitation at the resonance with the fundamental mode, where the stress level is slightly reduced (down to 80%, see Fig. 4b). The reason for this is the more pronounced contribution of higher frequencies (both the higher-frequency contribution of the fundamental and that of higher-order modes). Although the fundamental mode contributes substantially to the stress response, $S_{\sigma\sigma}$ is not dominated by that mode (Fig. 8b).

The stress level is almost the same as in the reference system at the displacement-optimal clearance g_{opt}. However, stress spikes occur which substantially exceed the reference stress level (Fig. 10). The high frequency modes contribute significantly to those spikes. Due to the fast time scale of the high-frequency modes, the spikes quickly decay. Subsequently, the response typically fluctuates around the reference response (no absorber) until the next impact occurs (Fig. 10b).

In the considered configuration, the location where the stress σ and the displacement q are monitored coincides with the location of the absorber. Another configuration was also investigated where the absorber was split into two equal masses, and symmetrically arranged at $x = L/5$ and $x = 4L/5$. Due to the symmetry, again, only the odd-ordered modes had to be considered in that case. Finally, the configuration with the absorber placed at $x = L/3$ was inves-

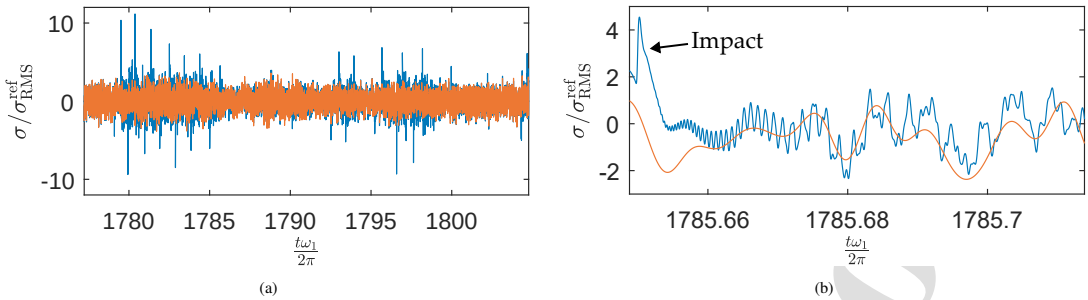

Figure 10: Typical stress response to broadband excitation: (a) representative time span with multiple impacts and (b) zoom into a representative time span with a single impact. Blue: System with absorber. Orange: reference system (without absorber).

tigated, for which the even-ordered modes become relevant. All results were qualitatively identical, including the transition of the stress level with the clearance from one linear limit case to the other (without falling below the reference). Also, the stress spikes remained. From this, it is concluded that the stress spikes and the poor performance of the absorber with respect to the stress level is not restricted to the absorber location considered here.

4.2. *Narrow-band excitation*

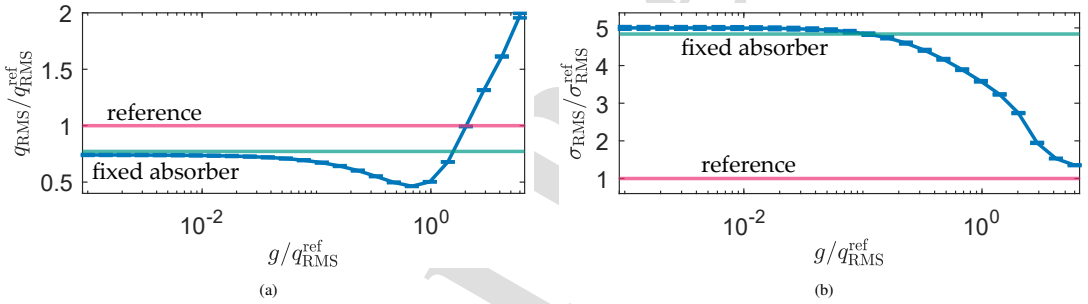

Figure 11: Response level vs. clearance under narrow-band forcing: (a) displacement level q_{RMS} and (b) stress level σ_{RMS}. The horizontal lines denote the respective linear limit cases of no (red) and fixed (green) absorber.

The excitation spectrum is now truncated more tightly around the central frequency by setting the bounds Ω_{min} and Ω_{max} to the limits of the band $\Omega_{\mathrm{c}} \pm 23.6\%$, spanning only the natural frequencies of modes 29 to 37. The displacement and the stress level are shown in Fig. 11 as function of the clearance. As in the case of broadband excitation, the displacement level is reduced by about factor two at an optimal clearance ($g_{\mathrm{opt}}/q_{\mathrm{RMS}}^{\mathrm{ref}} = 0.68$), and the stress level transitions between the linear limit cases without (significantly) exceeding or going below them. In contrast to the broadband case, the displacement level exceeds both linear limit cases at larger clearance.
The modal energy distribution is depicted in Fig. 13 for g_{opt} and for a large clearance. In the linear reference case, the fundamental mode still has the largest contribution, but it is far from being dominant. In fact, truncating the modal basis to only the modes within the half power bandwidth, i. e. modes 29 to 37, would still result in $0.47 \cdot q_{\mathrm{RMS}}(M = 221)$. This is also confirmed by the typical displacement response in Fig. 12, which has substantial high-frequency components, leading to a large number of significant impacts per fundamental period of $N_{\mathrm{sipp}} = 163$ in Fig. 12a and $N_{\mathrm{sipp}} = 152$ in Fig. 12b. In contrast to the broadband case, there is no clear impact pattern for g_{opt} (cf.Fig. 9)a. Still the absorber mitigates the contribution of the fundamental and the next few modes for g_{opt} (Fig. 13a). Apparently, the energy is scattered to higher-frequency modes, so that their contribution is increased (including the modes in the effective excitation spectrum). The reduced contribution of the low-frequency modes also leads to a reduced displacement level.

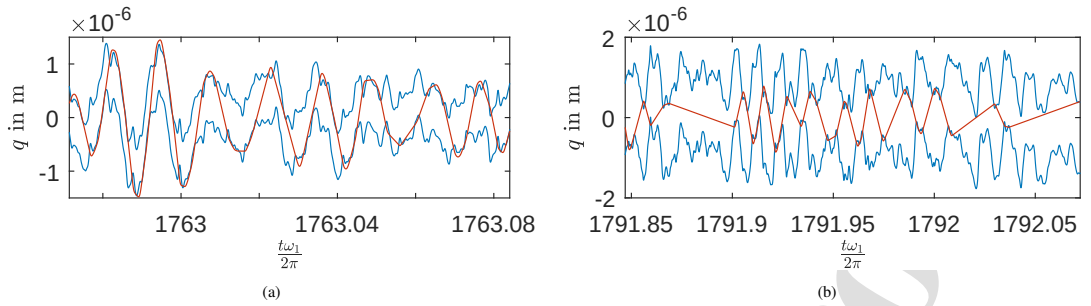

Figure 12: Representative movement of the absorber (red) inside the cavity walls (blue) under narrow-band excitation for (a) $g/q^{\mathrm{ref}}_{\mathrm{RMS}} = 0.5$ and (b) $g/q^{\mathrm{ref}}_{\mathrm{RMS}} = 1.0$.

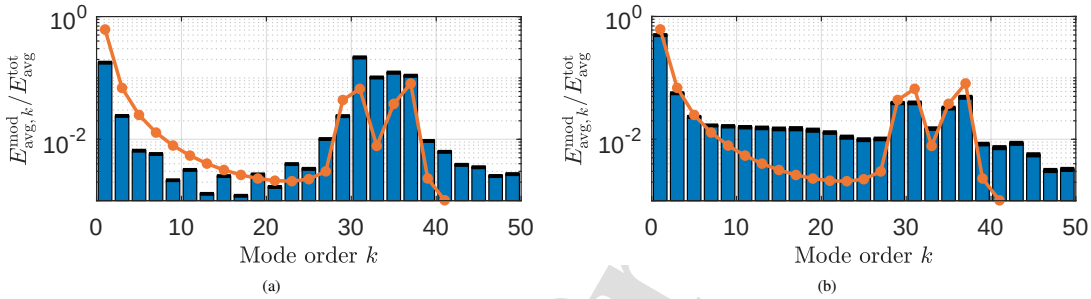

Figure 13: Modal energy distribution in the taut string under narrow-band excitation: (a) $g = g_{\mathrm{opt}}$ and (b) $g/q^{\mathrm{ref}}_{\mathrm{RMS}} = 6$. Blue: System with absorber. Orange: reference system (without absorber). Both systems are normalized with their respective $E^{\mathrm{tot}}_{\mathrm{avg}}$.

At larger clearance, the picture is quite different. The lowest few modes (1 to 7) and the modes in the excitation spectrum (29 to 37) have about the same energ contribution as in the reference case. Apparently, a substantial portion of the energy is scattered to the intermediate mode orders (9 to 27) and the modes beyond the excitation spectrum ($\geq$39). As in the case of harmonic excitation in resonance with mode 35, this is explained by the fact that the impacts occur less frequently and in a(n even) less regular manner for larger clearances, causing significant energy transfer from high to low frequencies. In accordance with Eq. (21), a certain amount of energy scattered to a lower-frequency mode is associated with a larger modal coordinate level, $\eta_{k,\mathrm{RMS}}$, and thus a larger displacement level. This explains that the displacement level is so large for wider clearance (Fig. 11a).

5. Conclusions

Based on the results obtained in this work, we conclude that the impact absorber tends to synchronize with the *displacement-dominant mode* (if any), for a certain clearance. In the considered case of the taut string, the fundamental mode was surprisingly prominent, even when the bandwidth of the excitation was limited to high mode orders (> 30). For an appropriate clearance, the absorber shows an optimum synchronization with that mode. Then, energy is scattered to frequencies higher than that of the displacement-dominant mode, and the displacement level is reduced. However, this reduction effect may be marginal, in particular, if there is no clearly dominating mode, but instead multiple modes (and frequencies) contribute substantially to the displacement response. Moreover, the optimum clearance depends sensitively on the form and level of the applied excitation; i. e., it is necessary to have good knowledge on the loading to achieve a high vibration mitigation effect. When higher mode orders contribute substantially to the displacement response, considerable high-to-low energy transfer occurs for clearances larger than that leading to optimum synchronization; this may result in a displacement level that exceeds the linear limit cases (no/fixed absorber). In summary, the impact absorber is more effective the narrower the excitation frequency bandwidth and the lower

Journal Pre-proof

the mode order. In contrast, the impact absorber is not well-suited for situations where multiple, possibly high-order modes contribute substantially to the displacement, as a result of high-frequency broadband excitation. Based on this, we do not expect that the impact absorber is useful for mitigating vortex-induced vibrations of transmission lines / stay cables in the turbulent regime, if the effective excitation spectrum spans only high-order modes. It should be remarked, however, that certain aspects of the problem setting considered in this work limit the transferability to that particular technical application (incl. spatial coherence of loading; variation of load level along span; positioning of absorber; performance measures).

The attachment of additional mass (absorber) induces a concentrated inertia load. In the case of the taut string, this led to a significant increase of the local stress level. This detrimental effect can only partly be compensated by the vibration mitigation effect, i. e. by limiting the power input to the system. Even in the case of resonant harmonic excitation of the fundamental mode, the stress level was only slightly decreased. In addition, the impacts cause stress spikes which typically exceed the linear limit cases. Finally, it should be recalled that the casing mass (and rotational inertia) was neglected in the present work; its addition is not expected to shift the above findings into a positive direction for the absorber.

Given the above stated critical conclusions on the impact absorber with regard to its broadband efficacy and its potentially detrimental effects on the stress, one may ask: *Is there a way out of the misery?* More specifically, under what conditions could the impact absorber still be useful, in particular for mitigating higher-order modes? The above findings should be accounted for by carefully designing the location and orientation of the absorber in such a way that the target mode (which shall be mitigated) should dominate the displacement at that location and in that direction. If there is more than one target mode, multiple absorbers are generally needed. The scattering of energy to high frequencies may generally have detrimental effects on the stress. Therefore, the high-frequency modes should not have their stress maxima in the fatigue-critical region of the structure. For the considered taut string, the stress maxima all coincided at the center, and this is where also the absorber was attached; this is of course not an ideal scenario for the impact absorber.

References

[1] A. F. Vakakis, O. V. Gendelman, G. Kerschen, L. A. Bergman, D. M. McFarland, and Y. S. Lee, *Nonlinear Targeted Energy Transfer in Mechanical and Structural Systems, Volumes I and II*. Springer Berlin Heidelberg, 2008.

[2] T. Theurich, J. Gross, and M. Krack, "Effects of modal energy scattering and friction on the resonance mitigation with an impact absorber," *Journal of Sound and Vibration*, vol. 442, pp. 71–89, 2019.

[3] M. Gzal, B. Fang, A. F. Vakakis, L. A. Bergman, and O. V. Gendelman, "Rapid non-resonant intermodal targeted energy transfer (imtet) caused by vibro-impact nonlinearity," *Nonlinear Dynamics*, vol. 101, no. 4, pp. 2087–2106, 2020.

[4] M. Gzal, A. F. Vakakis, L. A. Bergman, and O. V. Gendelman, "Extreme intermodal energy transfers through vibro-impacts for highly effective and rapid blast mitigation," *Communications in Nonlinear Science and Numerical Simulation*, vol. 103, p. 106012, 2021.

[5] T. Theurich, A. F. Vakakis, and M. Krack, "Predictive design of impact absorbers for mitigating resonances of flexible structures using a semi-analytical approach," *Journal of Sound and Vibration*, no. 516, p. 17pp, 2022.

[6] T. Theurich and M. Krack, "Experimental validation of impact energy scattering as concept for mitigating resonant vibrations," *Journal of Structural Dynamics*, no. 2, 2023.

[7] S. F. Masri and T. K. Caughey, "On the stability of the impact damper," *Journal of Applied Mechanics*, vol. 33, no. 3, pp. 586–592, 1966.

[8] C. N. Bapat and S. Sankar, "Single unit impact damper in free and forced vibration," *Journal of Sound and Vibration*, vol. 99, no. 1, pp. 85–94, 1985.

[9] P. Lieber, D. P. Jensen, *et al.*, "An acceleration damper: development, design and some applications," *Trans. ASME*, vol. 67, no. 10, pp. 523–530, 1945.

[10] M. R. Duncan, C. R. Wassgren, and C. M. Krousgrill, "The damping performance of a single particle impact damper," *Vibro-Impact Systems*, vol. 286, no. 1, pp. 123–144, 2005.

[11] E. Gourc, G. Michon, S. Seguy, and A. Berlioz, "Targeted energy transfer under harmonic forcing with a vibro-impact nonlinear energy sink: Analytical and experimental developments," *Journal of Vibration and Acoustics*, vol. 137, no. 3, pp. 031008–031008–7, 2015.

[12] E. Gourc, S. Seguy, G. Michon, A. Berlioz, and B. P. Mann, "Quenching chatter instability in turning process with a vibro-impact nonlinear energy sink," *Journal of Sound and Vibration*, vol. 355, pp. 392–406, 2015.

[13] T. Li, E. Gourc, S. Seguy, and A. Berlioz, "Dynamics of two vibro-impact nonlinear energy sinks in parallel under periodic and transient excitations," *International Journal of Non-Linear Mechanics*, vol. 90, pp. 100–110, 2017.

[14] C.-H. Lamarque, O. V. Gendelman, A. Ture Savadkoohi, and E. Etcheverria, "Targeted energy transfer in mechanical systems by means of non-smooth nonlinear energy sink," *Acta Mechanica*, vol. 221, no. 1, p. 175, 2011.

[15] O. V. Gendelman, "Analytic treatment of a system with a vibro-impact nonlinear energy sink," *Journal of Sound and Vibration*, vol. 331, no. 21, pp. 4599–4608, 2012.

[16] A. L. Paget, "Vibration in steam turbine buckets and damping by impacts," *Engineering*, vol. 143, pp. 305–307, 1937.

Journal Pre-proof

[17] M. A. Al-Shudeifat, A. F. Vakakis, and L. A. Bergman, "Shock mitigation by means of low- to high-frequency nonlinear targeted energy transfers in a large-scale structure," *Journal of Computational and Nonlinear Dynamics*, vol. 11, no. 2, pp. 1–11, 2015.
[18] T. Li, S. Seguy, and A. Berlioz, "Optimization mechanism of targeted energy transfer with vibro-impact energy sink under periodic and transient excitation," *Nonlinear Dynamics*, pp. 1–19, 2016.
[19] O. Gendelman and A. Alloni, "Dynamics of forced system with vibro-impact energy sink," *Journal of Sound and Vibration*, vol. 358, pp. 301–314, 12 2015.
[20] J. P. Den Hartog, *Mechanical vibrations*. Courier Corporation, 1985.
[21] T. Detroux, G. Habib, L. Masset, and G. Kerschen, "Performance, robustness and sensitivity analysis of the nonlinear tuned vibration absorber," *Mechanical Systems and Signal Processing*, vol. 60-61, pp. 799–809, 2015.
[22] C.-J. Kim, "Design sensitivity analysis of a stockbridge damper to control resonant frequencies," *Journal of Mechanical Science and Technology*, vol. 31, pp. 4145–4150, 9 2017.
[23] Z. Wang, H.-N. Li, and G. Song, "Aeolian vibration control of power transmission line using stockbridge type dampers — a review," *International Journal of Structural Stability and Dynamics*, vol. 21, p. 2130001, 1 2021.
[24] F. Di, L. Sun, L. Qin, L. Chen, Y. Zou, L. Jiang, and Y. Zhu, "Full-scale experimental study on vibration control of bridge suspenders using the stockbridge damper," *Journal of Bridge Engineering*, vol. 25, 8 2020.
[25] N. Meyer and R. Seifried, "Numerical and experimental investigations in the damping behavior of particle dampers attached to a vibrating structure," *Computers and Structures*, vol. 238, 2020.
[26] R. Chabrier, G. Chevallier, E. Foltête, and E. Sadoulet-Reboul, "Experimental investigations of a vibro-impact absorber attached to a continuous structure," *Mechanical Systems and Signal Processing*, vol. 180, 11 2022.
[27] P. Hagedorn, "On the computation of damped wind-excited vibrations of overhead transmission lines," *Journal of Sound and Vibration*, vol. 83, pp. 253–271, 1982.
[28] U. Starossek, "Cable dynamics - a review," *Structural Engineering International*, vol. 4, pp. 171–176, 8 1994.
[29] V. Denoël and T. Andrianne, "Real-scale observations of vortex induced vibrations of stay-cables in the boundary layer," *Procedia Engineering*, vol. 199, pp. 3109–3114, 2017.
[30] R. K. R. Tumkur, R. Calderer, A. Masud, A. J. Pearlstein, L. A. Bergman, and A. F. Vakakis, "Computational study of vortex-induced vibration of a sprung rigid circular cylinder with a strongly nonlinear internal attachment," *Journal of Fluids and Structures*, vol. 40, pp. 214–232, 7 2013.
[31] A. Blanchard, L. A. Bergman, and A. F. Vakakis, "Targeted energy transfer in laminar vortex-induced vibration of a sprung cylinder with a nonlinear dissipative rotator," *Physica D: Nonlinear Phenomena*, vol. 350, pp. 26–44, 7 2017.
[32] B. Vickery and A. Clark, "Lift or across- wind response of tapered stacks," *ASCE J Struct Div*, vol. 98, pp. 1–20, 1972.
[33] F. Gehr, T. Theurich, C. Monjaraz-Tec, J. Gross, S. Schwarz, A. Hartung, and M. Krack, "Computational and experimental analysis of the impact of a sphere on a beam and the resulting modal energy distribution," *Mechanical Systems and Signal Processing*, vol. 180, p. 109407, 2022.
[34] L. Carassale and G. Solari, "Monte carlo simulation of wind velocity fields on complex structures," *Journal of Wind Engineering and Industrial Aerodynamics*, vol. 94, pp. 323–339, 2006.
[35] M. Shinozuka and C.-M. Jan, "Digital simulation of random processes and its applications," *Journal of Sound and Vibration*, pp. 111–128, 1972.
[36] R. K. Roy, R. D. Rocke, and J. E. Foster, "Application of impact dampers to continuous systems," *American Society of Mechanical Engineers (Paper)*, no. 75 -DET-81, pp. 1317–1324, 1975.
[37] R. Chalmers and S. E. Semercigil, "Impact damping the second mode of a cantilevered beam," *Journal of Sound and Vibration*, vol. 146, no. 1, pp. 157–161, 1991.
[38] Butt Aamir S. and Akl Fred A., "Experimental analysis of impact-damped flexible beams," *Journal of Engineering Mechanics*, vol. 123, no. 4, pp. 376–383, 1997.
[39] J. Cheng and H. Xu, "Inner mass impact damper for attenuating structure vibration," *International Journal of Solids and Structures*, vol. 43, no. 17, pp. 5355–5369, 2006.
[40] K. Li and A. P. Darby, "An experimental investigation into the use of a buffered impact damper," *Journal of Sound and Vibration*, vol. 291, no. 3-5, pp. 844–860, 2006.
[41] K. Li and A. P. Darby, "A buffered impact damper for multi-degree-of-freedom structural control," *Earthquake Engineering & Structural Dynamics*, vol. 37, no. 13, pp. 1491–1510, 2008.
[42] R. Vinayaravi, D. Kumaresan, K. Jayaraj, A. K. Asraff, and R. Muthukumar, "Experimental investigation and theoretical modelling of an impact damper," *Vibro-Impact Systems*, vol. 332, no. 5, pp. 1324–1334, 2013.
[43] W. Yang, Y. Seong, S. Jeong, and J. Park, "Vibration reduction using meta-structures composed of tuned dynamic absorbers employing mass impacts," *Composite Structures*, vol. 183, no. 1, pp. 216–220, 2017.
[44] Y. Yang and X. Wang, "Investigation into the linear velocity response of cantilever beam embedded with impact damper," *JVC/Journal of Vibration and Control*, vol. 25, no. 7, pp. 1365–1378, 2019.
[45] B. Fang, T. Theurich, M. Krack, L. A. Bergman, and A. F. Vakakis, "Vibration suppression and modal energy transfers in a linear beam with attached vibro-impact nonlinear energy sinks," *Communications in Nonlinear Science and Numerical Simulation*, vol. 91, p. 105415, 2020.
[46] P. J. Gonçalves, A. Peplow, and M. J. Brennan, "Exact expressions for numerical evaluation of high order modes of vibration in uniform euler-bernoulli beams," *Applied Acoustics*, vol. 141, pp. 371–373, 12 2018.

Appendix A. Modes of the taut string

To determine the modes of the taut string, the underlying autonomous form of Eq. (1) without the effect of the absorber is considered, i. e. $f(t) = 0 = \lambda$. Substitution of the ansatz $w(x,t) = \varphi(x/L)\eta(t)$ into the partial differ-

Journal Pre-proof

ential equation and separation of variables yields two ordinary differential equations, one with t and one with x as independent variable. The first is the harmonic oscillator equation, $\ddot{\eta}+\omega^2\eta=0$. The second is

$$\varphi''''-\frac{TL^2}{EI}\varphi''-\frac{EI}{\mu L^4}\varphi=0\,, \tag{A.1}$$

where $\square'=\partial\square/\partial\xi$ with $\xi=x/L$. This equation is autonomous, linear in the sought mode shape φ and has constant coefficients. Using the exponential ansatz $\tilde{\varphi}=\mathrm{e}^{\lambda\xi}$, leads to the characteristic (algebraic) equation

$$\lambda^4-\frac{TL^2}{EI}\lambda^2-\frac{\omega^2\mu L^4}{EI}=0\,, \tag{A.2}$$

which can be solved for λ^2 as

$$\lambda^2=\frac{L^2}{2EI}\left(T\mp\sqrt{T^2+4\mu EI\omega^2}\right). \tag{A.3}$$

Note that both λ and ω are unknown at this point, and are determined later, when the general solution is appropriated to the boundary conditions. Since EI, T and μ are all positive (and L, ω are all real), the first solution of Eq. (A.3) (with *minus* before the root) yields a pair of imaginary solutions for λ, whereas the second (with *plus* before the root) yields a pair of real solutions:

$$\lambda_{1,2} = \pm\mathrm{i}A\,, \tag{A.4}$$
$$\lambda_{3,4} = \pm B\,, \tag{A.5}$$
$$A(\omega) = \sqrt{\frac{L^2}{2EI}\left(\sqrt{T^2+4\mu EI\omega^2}-T\right)}\,, \tag{A.6}$$
$$B(\omega) = \sqrt{\frac{L^2}{2EI}\left(\sqrt{T^2+4\mu EI\omega^2}+T\right)}\,. \tag{A.7}$$

With this, the general solution for φ is

$$\varphi = \Re\{\tilde{\alpha}_1\mathrm{e}^{+\mathrm{i}A\xi}+\tilde{\alpha}_2\mathrm{e}^{-\mathrm{i}A\xi}+\tilde{\alpha}_3\mathrm{e}^{+B\xi}+\tilde{\alpha}_4\mathrm{e}^{-B\xi}\}\,, \tag{A.8}$$
$$= \alpha_1\sin(A\xi)+\alpha_2\cos(A\xi)+\alpha_3\cosh(B\xi)+\alpha_4\sinh(B\xi)\,, \tag{A.9}$$

with the real coefficients α_1 to α_4.
The general solution expressed in Eq. (A.9) still needs to be adjusted to the boundary conditions specified in Eqs. (2)-(5). This yields the equations:

$$\varphi(0) = 0\,, \tag{A.10}$$
$$\varphi(1) = 0\,, \tag{A.11}$$
$$\frac{EI}{L^2}\varphi''(0)+\frac{J\omega^2}{L}\varphi'(0) = 0\,, \tag{A.12}$$
$$\frac{EI}{L^2}\varphi''(1)-\frac{J\omega^2}{L}\varphi'(1) = 0\,, \tag{A.13}$$

where it was used that $\partial^2 w/\partial t^2=\varphi\ddot{\eta}=-\varphi\omega^2\eta$. Substituting Eq. (A.9) into Eqs. (A.10)-(A.13) yields a homogeneous system of four linear algebraic equations. This can be summarized as $\boldsymbol{C}\boldsymbol{\alpha}=\boldsymbol{0}$ with respect to the coefficients $\boldsymbol{\alpha}=[\alpha_1;\alpha_2;\alpha_3;\alpha_4]$ and the 4×4-matrix $\boldsymbol{C}$. Non-trivial solutions ($\boldsymbol{\alpha}\neq\boldsymbol{0}$) require $\det\boldsymbol{C}=0$, which leads to:

$$\begin{aligned}\sin(A)\sinh(B)\left(EI^2\left(A^2+B^2\right)^2-J^2L^2\omega^4\left(A^2-B^2\right)\right)+2J^2L^2\omega^4AB\left(1-\cos(A)\cosh(B)\right)\\ +2EIJL\omega^2\left(A^2+B^2\right)\cdot\left(A\cos(A)\sinh(B)-B\sin(A)\cosh(B)\right)=0\,.\end{aligned} \tag{A.14}$$

Since $A(\omega)$ and $B(\omega)$ according to Eq. (A.6) and Eq. (A.7), Eq. (A.14) governs the natural (angular) frequencies ω (*frequency equation*). For each natural frequency, $\boldsymbol{\alpha}$ follows from the rank deficient algebraic equation system. The solution is

$$\alpha_1 = 1\,, \tag{A.15}$$

$$\alpha_2 = \frac{JL\omega^2\left(A\sinh(B) - B\sin(A)\right)}{EI\sinh(B)\left(A^2+B^2\right) + JLB\omega^2\left(\cos(A) - \cosh(B)\right)}\,, \tag{A.16}$$

$$\alpha_3 = -a_2\,, \tag{A.17}$$

$$\alpha_4 = \frac{JL\omega^2\left(\cosh(B) - \cos(A)\right) - EI\sin(A)\left(A^2+B^2\right)}{EI\sinh(B)\left(A^2+B^2\right) + JLB\omega^2\left(\cos(A) - \cosh(B)\right)}\,. \tag{A.18}$$

These coefficients define the mode shape corresponding to ω in accordance with Eq. (A.9).
For low mode orders, the bending stiffness is less relevant than the preload effect ($T^2 \gg 4EI\mu\omega^2$ in Eq. (A.3)), so that the mode shapes and natural frequencies resemble those of the ideal taut string. For high mode orders, the opposite is the case ($T^2 \ll 4EI\mu\omega^2$), so that the preload has negligible effect and the frequencies resemble those of a beam without pre-stress. Moreover, the rotational inertia, J, becomes dominant and imposes a zero slope $\varphi'(0), \varphi'(1) \to 0$. Thus, the mode shapes and natural frequencies converge to those of a clamped-clamped beam (without preload).
The expressions in Eqs. (A.16) and (A.18) lead to large round-off errors for high mode orders. From mode order 89 on, this effect is no longer negligible. To overcome this, the mathematically equivalent but numerically stable evaluation of the mode shapes involving exponential instead of hyperbolic functions is adopted from [46].

Ideal taut string

For the interpretation of some of the results, it is useful to consider the closed-form expressions obtained for the case of an ideal taut string (no bending stiffness, $EI = 0$, no rotational moment at the boundary, $J = 0$). In this case,

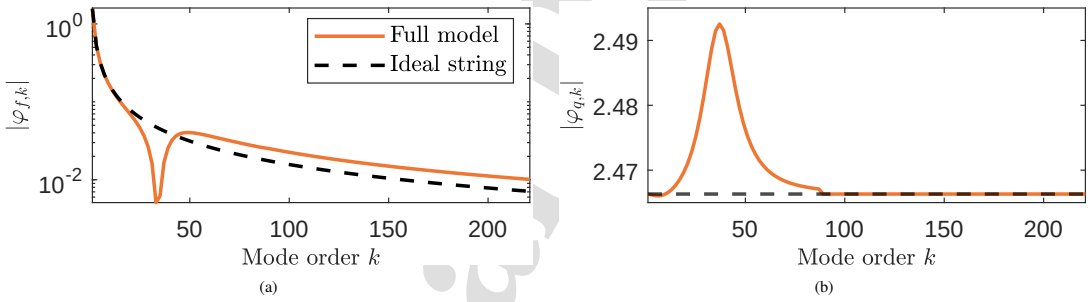

Figure A.14: Comparison between $\varphi_{f,k}$ and $\varphi_{q,k}$ for the full linear system (orange) and the ideal taut string (black).

we have

$$\omega_k = k\pi\sqrt{\frac{T}{\mu L^2}}\,, \tag{A.19}$$

$$\varphi_k = \sqrt{\frac{2}{\mu L}}\sin(k\pi\xi)\,. \tag{A.20}$$

Journal Pre-proof

Journal Pre-proof

$$\varphi_{f,k} = -\frac{2}{k\pi}\sqrt{\frac{2}{\mu L}}, \tag{A.21}$$

$$\varphi_{q,k} = \sqrt{\frac{2}{\mu L}}\begin{cases} 0 & k \text{ even} \\ +1 & \frac{k+1}{2} \text{ odd} \\ -1 & \frac{k+1}{2} \text{ even} \end{cases}, \tag{A.22}$$

$$\varphi_{\sigma,k} = |y|_{\max}\frac{E}{L^2}\sqrt{\frac{2}{\mu L}}(k\pi)^2. \tag{A.23}$$

A comparison between this approximation and the full model with finite rotational inertia and bending stiffness $EI, J > 0$ for $\varphi_{f,k}$ and $\varphi_{q,k}$ is shown in Fig. A.14. As expected, the approximation yields good results for low mode orders.
Finally, the claim made in Subsection 3.1, that an energy transfer from the fundamental to a higher frequency increases the stress level, shall be proven. When the fundamental mode is driven near its natural frequency $\Omega \approx \omega_1$, we have (cf.Eq. (21)):

$$E^{\text{mod}}_{\text{avg},1} = \frac{1}{4}\left(\omega_1^2 + \Omega^2\right)|\hat{\eta}_1|^2 \approx \frac{1}{2}\omega_1^2|\hat{\eta}_1|^2. \tag{A.24}$$

As the high-frequency modes are driven off resonance, their behavior is dominated by their free response. Under light damping, the energy of mode $k \gg 1$ is

$$E^{\text{mod}}_{\text{avg},k} \approx \frac{1}{2}\omega_k^2|\hat{\eta}_k|^2. \tag{A.25}$$

Suppose that energy is transferred instantaneously from mode 1 to mode k, $E^{\text{mod}}_{\text{avg},1} = E^{\text{mod}}_{\text{avg},k}$. Then we have

$$|\hat{\eta}_k| = \frac{1}{k}|\hat{\eta}_1|, \tag{A.26}$$

where $\omega_k/\omega_1 = k$ was used (Eq. (A.19)). The stress is $\sigma = \sum_{k=1}^{M}\varphi_{\sigma,k}\eta_k$, where $\varphi_{\sigma,k} \sim k^2$ (Eq. (A.23)). Thus, by transferring energy from mode 1 to mode k, the stress is increased by factor $k^2 \cdot 1/k = k$.

Appendix B. Test rig; model updating

In this appendix, the test rig of the taut string and the model updating procedure are described. The identified parameters are used in the model of the host structure as described in Section 2.
The test rig is illustrated in Fig. B.15a. It consists of a bass piano string that is clamped inside a pin at each end. The pins are mounted via roller bearings. Thus, the rotation of the string is not constrained, but it is associated with a certain rotational moment of inertia. The string itself is made of a steel core with a double copper winding around the core (Fig. B.15b). The copper winding increases the lineic mass without substantially increasing the bending stiffness. With this, the fundamental natural frequency is decreased and the next higher-order natural frequencies are close to being integer multiples. For its original purpose inside of a piano, the latter leads to a more consonant perception of the string's sound by the human ear. The relatively small bending stiffness is also desired in the test rig, as this makes it more representative of a real stay cable or transmission line, whose bending stiffness is typically negligible [28, 29]. A similar effect could have been achieved by using a longer string, which was not feasible due to the limited dimensions of the shaker table, or by using a thinner string, which would have made the instrumentation and the planned equipment with an absorber device difficult to impossible (miniaturization needed).
The length L is defined by the geometry and placement of the clamping devices. The lineic mass μ was determined by weighing the string and dividing by its length. The preload is applied via a free weight, so that the tensile load T is equal to the gravitational force; the mass of the free weight was measured as 20.9 kg. All remaining parameters (EI, J, D_k) were identified based on the results of an experimental (linear) modal analysis as explained next.
For the modal test, the system was placed onto the slip table of a large shaker (TIRA TV 51010/LS-340; 11 kN nominal sine force). Thus, the string undergoes base excitation, whereas it is exposed to a uniform forcing in the model

Journal Pre-proof

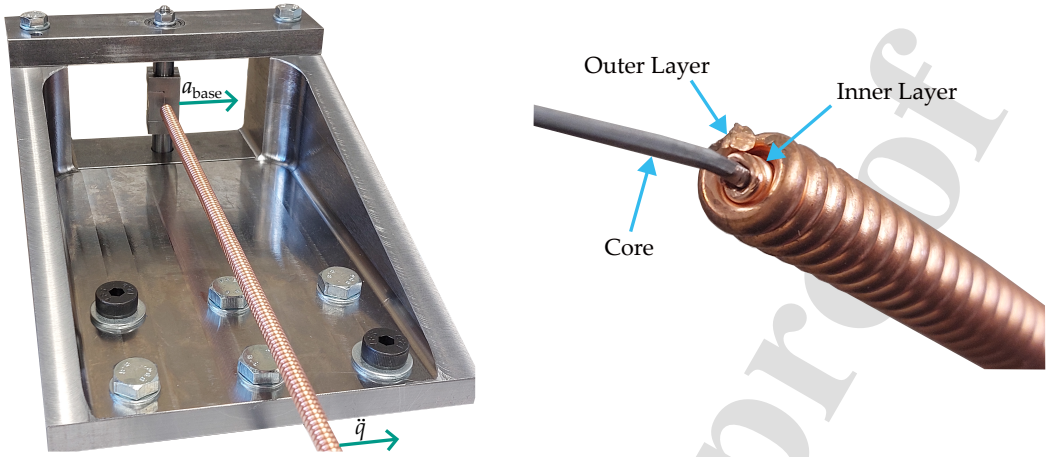

(a) (b)

Figure B.15: Piano string test rig: (a) Overview and clamping; (b) Close view of the piano string showing the steel core and its two layers of copper winding.

described by Eq. (1). The base excitation is consistently accounted for in the model by setting $f(t) = \mu \cdot a(t)$, where a is the base acceleration, and redefining w as the displacement relative to the base. The base motion is determined by a laser Doppler vibrometer (Polytec OFV-5000/OFV-552), and the response of the string is determined by a uni-axial accelerometer (PCB Piezotronics 352C22) glued at the center of the string (mass in order of 10^{-3} kg considered negligible compared to 0.329 kg of string). The base acceleration a was determined by numerical differentiation of the measured velocity, and the relative acceleration $\ddot{q}$ by subtracting a from the measured absolute acceleration. A dSpace MircroLabBox was used for data acquisition and also to feed a voltage signal into the shaker's amplifier.
The string was exposed to a broadband random base acceleration, with a power spectral density S_{aa} of the same form as in Eq. (15). The level was set to $a_{\text{RMS}} = f_{\text{RMS}}/\mu$. The transfer behavior from the shaker amplifier's voltage input to the base acceleration is not a priori known. The power spectral density function of the voltage was determined in an iterative process, so that the target S_{aa} was achieved with reasonable accuracy. The voltage time series was generated with the same algorithm as in the stochastic simulation.
From the obtained time series of base acceleration a and relative acceleration of the string's center $\ddot{q}$, the frequency response function is estimated as

$$G_{\ddot{q}a}(\Omega) = \frac{S_{\ddot{q}a}(\Omega)}{S_{aa}(\Omega)}\,, \tag{B.1}$$

where $S_{\ddot{q}a}$ is the cross spectral density function between $\ddot{q}$ and a. From $G_{\ddot{q}a}(\Omega)$, the frequencies and damping ratios D_k of the odd-ordered modes from $k = 1$ to $k = 49$ were identified using the Polyreference Least-Squares Complex Frequency Domain (p-LSCF) algorithm in m+p Analyzer. The identified damping ratios are directly adopted; for $k > 49$ the value $D_k = 0.2$ % was used. The string's bending stiffness EI and the clamping's rotational inertia J were selected in such a way that the error norm ε_ω,

$$\varepsilon_\omega = \sum_{k=1}^{49} \left(\omega_k - \overline{\omega}_k\right)^2\,, \tag{B.2}$$

is minimized, where ω_k is the solution of Eq. (A.14) and $\overline{\omega}_k$ is the experimentally identified value.
All identified parameters are listed in Tab. 1. To assess the quality of the updated string model, the computed frequency response function is compared against the experimentally identified reference in Fig. B.16. The agreement is quite satisfactory, especially in view of the very wide frequency band, which spans from the fundamental up to the 49-th

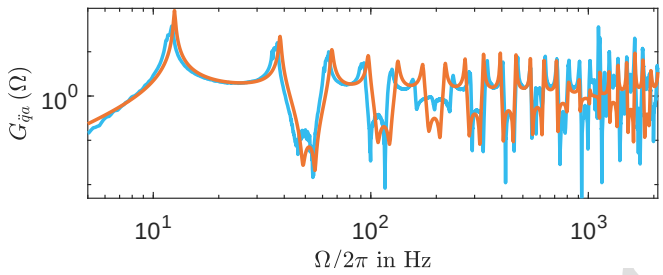

Figure B.16: Frequency response function $G_{\ddot{q}a}(\Omega)$: updated model (orange) vs. experimentally identified reference (blue).

mode. The larger discrepancy around 1 kHz could be due to the dynamics of the clamping, and/or the breakdown of the considered beam theory, which assumes a homogeneous cross section area (and the wave lengths are no longer negligibly small compared to the cross section dimensions).

Journal Pre-proof

Journal Pre-proof

- Impact absorber shows unexpectedly limited broadband efficacy.
- Under broadband excitation, multiple modes may dominate the displacement.
- Then the absorber does not synchronize well with any/all of those modes.
- Also, high-to-low energy transfer may occur for larger clearances.
- In addition, detrimental effects on the stress are possible.

Journal Pre-proof

Journal Pre-proof

Weidemann: Software; Validation; Formal analysis; Investigation; Data Curation; Writing - Original Draft; Visualization
Carassale: Conceptualization; Methodology; Software; Writing - Review & Editing
Denoel: Conceptualization; Methodology; Writing - Review & Editing
Krack: Conceptualization; Methodology; Resources; Writing - Review & Editing

Journal Pre-proof

Declaration of interests

☒ The authors declare that they have no known competing financial interests or personal relationships that could have appeared to influence the work reported in this paper.

☐The authors declare the following financial interests/personal relationships which may be considered as potential competing interests:

Journal Pre-proof